# COOPERATIVE TRANSPORTATION OF A CABLE–SUSPENDED LOAD USING ROTORCRAFT: A MINIMAL SWING APPROACH

Elia Costantini[1], Emanuele L. de Angelis[*,2], Fabrizio Giulietti[3]

*University of Bologna, Department of Industrial Engineering (DIN), CIRI Aerospace, Forlí, Italy 47121*

**Abstract**

In this paper cooperative transportation of a cable–suspended load by two rotorcraft is analyzed. A control law is proposed that allows the agents in the formation to simultaneously perform trajectory–tracking, formation geometry keeping, and payload swing stabilization. The controller is generated for a system made of three point masses and a set of two linear–elastic cables, according to Newton–Euler approach. A proof of local exponential stability is derived for closed–loop system with the requirement that the loaded formation exhibits a two–time–scale behavior: the fast dynamics develops with formation geometry stabilization and payload swing damping while the slow dynamics characterizes the trajectory–tracking task. Validation is performed in a realistic simulation scenario where multirotors are modeled as rigid bodies under the effect of external disturbances and rotor–generated forces and moments obtained by Blade Element Theory approach. The proposed method has the merit of relative simplicity and is shown to significantly improve vehicle flying qualities while minimizing hazardous payload oscillations.

## 1. INTRODUCTION

In recent years unmanned aerial platforms such as multirotors and helicopters have been widely investigated by academic and industrial research groups. The multirotor configuration, in particular, represents the most popular solution for aerial applications due to incomparable features in terms of mechanical simplicity, controllability, and easy handling in narrow areas (Ref. 1). Along with these configuration–related advantages, the technical advancement of electric propulsion systems and the growing availability of miniaturized high–performance electronics have contributed to the widespread adoption of multirotors from hobby to industrial applications. Common applications include photography and videography, inspection and mapping, precision farming, law enforcement, and payload delivery (Ref. 2).

While envisaging complex Air Mobility and Delivery (AMD) scenarios, two approaches are typically considered. The former consists in providing vehicles with graspers or a sufficiently large cargo compartment, leading to increased take–off mass and complexity, reduced flight endurance and range, and typically degraded agility (Refs. 3 and 4). The latter approach consists in the equipment of cable–suspended loads, which relatively preserves the performance of the rotorcraft and the simplicity of systems, but it introduces additional non–actuated degrees of freedom inherently related to the swing motion (Ref. 5). In this respect, it is a fact that the payload induces disturbance forces and moments that can significantly affect the motion of the lifting vehicle. At the same time, the oscillations may damage the payload or its environment by colliding with obstacles.

The problem of a single rotorcraft carrying a load has been addressed in the literature considering minimal swing. In Ref. 6 the authors explore the effect of dynamic load disturbances introduced by an instantaneously–increased payload mass and how this affects a quadrotor under proportional–integral–derivative flight control. In Ref. 7 the authors develope an adaptive controller to respond to changes in the multirotor center of gravity. An adaptive controller for a quadrotor transporting a payload connected through a flexible cable is presented in Ref. 8. The cable is modeled as a set of serially–connected rigid links and the payload is described as a point–mass. A hybrid approach is investigated in Ref. 9 to model the multirotor–payload system and handle wire collapse, provided that trajectory controllers stabilize the load position in 2D environment. A nested saturation controller to stabilize the system and control the oscillations is proposed in Ref. 10. In such a framework the control law guarantees asymptotic stability without any restrictions on the position and velocity of the aerial vehicle. In Ref. 11

[*]Corresponding author
[1]Ph.D. Student, elia.costantini3@unibo.it
[2]Assistant Professor, emanuele.deangelis4@unibo.it
[3]Associate Professor, fabrizio.giulietti@unibo.it

the authors introduce a nonlinear controller to stabilize the quadrotor and the load during positioning and trajectory–tracking tasks. Input–shape filtering methods are also used to generate a reference trajectory that minimizes residual swing during maneuvers (Ref. 12). Finally, in a recent work by one of the authors of the present paper (Ref. 13), a set of (inner–loop) controllers is assumed to stabilize the hovering condition of an isolated multirotor with prescribed dynamic behavior. Provided the vehicle is equipped with the suspended load, a set of auxiliary (outer–loop) controllers is proposed to provide the complete system with a set of desired dynamic properties, specified also for the oscillatory mode.

Although the use of a single agent is relatively simple, there are transportation tasks that can only be performed by flexible and scalable multi–agent systems, such as carrying a load heavier than the payload capacity of the single vehicle or successfully deliver an object under a vehicle failure. In this respect, cooperative load transportation has been studied in many papers. In Ref. 14 a PID controller is developed to address the transportation of a common object with quadrotors via cables. However, the proposed control method is proven to suffer from the inability to reduce oscillations in the underdamped system. In Ref. 15 the authors develop a LQR controller combined with a Kalman filter for cooperative load transportation using two agents. Validation is performed experimentally by using two commercial quadrotors equipped with ultrasound altimeter, IMU, and frontal cameras. In Ref. 16 a hierarchical control scheme is designed for two quadrotors carrying a slung payload. In particular, a linear controller is adopted for position loop while a quaternion–based nonlinear controller characterizes the attitude loop. Finally, the authors validate the proposed approach for both a rigid and a flexible wire by numerical simulations. In the case of an unknown mass, a cooperative algorithm robust to environmental disturbances is investigated in Ref. 17. The proposed control algorithm is designed according to decentralized architecture where each quadrotor utilizes relative velocity and position of its neighbors to reach desired formation shapes. A decentralized Lyapunov–based controller is also presented for aerial co–manipulation of a cable–suspended payload with two aerial robots in Ref. 18.

Athough previous papers have presented different types of control algorithms to solve the cooperative transportation control problems, a generalized approach is still lacking in the literature that simultaneously satisfies requirements in terms of 1) formation geometry–keeping, 2) trajectory–tracking, and 3) payload swing damping for 4) a generic rotary–wing configuration (helicopter or multirotor). In this paper, a novel control strategy is thus proposed to convert the cooperative load transportation problem to the stabilization of a formation where the dynamics of the suspended load is treated as an external disturbance. Starting from the results of a recent work by some of the authors (Ref. 19), a formation control scheme is proposed for a formation of two agents with the aim to perform trajectory–tracking and formation geometry–keeping with the additional stabilization of the oscillatory dynamics. Stemming from the idea presented in Ref. 20, controller gains are designed so that the loaded formation exhibits a two–time–scale behavior: the fast dynamics develops with simultaneous formation geometry stabilization and payload swing damping while the slow dynamics is related to the trajectory–tracking task. Under these conditions, the basic results of singular perturbation theory are evoked for both the proof of stability and the preliminary design of control gains. It is stressed that the proof of stability is based on conservative results, derived from converse Lyapunov theorems (Ref. 21). Hence, the given requirements on forced time separation can be relaxed in many practical applications.

The derivation of the controller is based on a set of simplifying assumptions that include the modeling of both the lifting vehicles and the load as a point–mass, according to the Eulerian method. The validity of the approach and the performance of the controller are evaluated by means of numerical simulations applied to a realistic test case, where a formation made of two multirotor vehicles is detailed in terms of electric propulsion system components and blade element characterization of propellers. A test case is proposed in a non–nominal scenario in the presence of environmental disturbances and model uncertainties.

Despite the highly–nonlinear structure of proposed control scheme, the approach is simple and gives the reader a deep insight into the physical system. In this direction, the generation of a two–time–scale behavior is not only performed in view of the stability proof but it allows to favorably address the typical requirements on slung–load mission tasks, where trajectory tracking needs to be performed after a fast and effective damping of load oscillations.

## 2. PROBLEM STATEMENT AND SOLUTION

Starting from the definition of reference frames, a $3$ degrees–of–freedom mathematical model is adopted to describe both the rotorcraft and the load. After formulating the control problem, numerical validation is performed by considering the $i$–th multirotor as a rigid body with center of gravity in $P_i$. The two vehicles (including suspension cables) are assumed to be identical.

### 2.1. Reference frames

Three right–handed orthogonal reference frames are introduced:

1. an Earth-fixed North-East-Down frame, $\mathcal{F}_E = \{O_E; \boldsymbol{x}_E, \boldsymbol{y}_E, \boldsymbol{z}_E\}$: the origin, $O_E$, is arbitrarily fixed to a point on the Earth's surface, $\boldsymbol{x}_E$ aims in the direction of geodetic North, $\boldsymbol{z}_E$ points downward along the Earth ellipsoid normal, and $\boldsymbol{y}_E$ completes a right-handed triad. This frame is assumed to be inertial under the assumption of flat and non–rotating Earth;

2. two Body–fixed frames, $\mathcal{F}_{Bi} = \{P_i; \boldsymbol{x}_{Bi}, \boldsymbol{y}_{Bi}, \boldsymbol{z}_{Bi}\}$, $i = 1, 2$: the longitudinal axis $\boldsymbol{x}_{Bi}$ is positive out the nose of the $i$–th rotorcraft in its selected plane of symmetry, $\boldsymbol{z}_{Bi}$ aims in the direction of fuselage/frame belly, and $\boldsymbol{y}_{Bi}$ completes a right–handed triad;

3. a rotorcraft structural reference frame, $\mathcal{F}_S = \{O_S; \boldsymbol{x}_S, \boldsymbol{y}_S, \boldsymbol{z}_S\}$, used to locate $CG$ and all vehicle components: the axes are parallel to the body–fixed frame axes, such that $\boldsymbol{x}_S = -\boldsymbol{x}_B$, $\boldsymbol{y}_S = \boldsymbol{y}_B$, and $\boldsymbol{z}_S = -\boldsymbol{z}_B$. The origin is located at some arbitrary point within the rotorcraft plane of symmetry. Stations ($ST$) are measured positive aft along the longitudinal axis. Buttlines ($BL$) are lateral distances, positive to the right, and waterlines ($WL$) are measured vertically, positive upward.

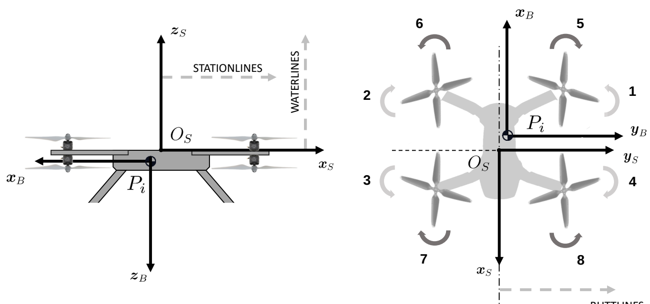


Figure 1: Multirotor body–fixed reference frames.

A sketch of the $i$–th rotorcraft including the selected reference frames is reported in Figure 1.

Let $s(\cdot) = \sin(\cdot)$ and $c(\cdot) = \cos(\cdot)$. Vector transformation between $\mathcal{F}_E$ and $\mathcal{F}_{Bi}$ is provided by rotation matrix (Ref. 13):

$$\text{(1)}\quad \boldsymbol{T}_{BE}(\boldsymbol{\alpha}_i) = \begin{bmatrix} c\theta_i\, c\psi_i & c\theta_i\, s\psi_i & -s\theta_i \\ s\phi_i\, s\theta_i\, c\psi_i - c\phi_i\, s\psi_i & s\phi_i\, s\theta_i\, s\psi_i + c\phi_i\, c\psi_i & s\phi_i\, c\theta_i \\ c\phi_i\, s\theta_i\, c\psi_i + s\phi_i\, s\psi_i & c\phi_i\, s\theta_i\, s\psi_i - s\phi_i\, c\psi_i & c\phi_i\, c\theta_i \end{bmatrix}$$

obtained by a 3-2-1 Euler rotation sequence where $\boldsymbol{\alpha}_i = [\phi_i,\, \theta_i,\, \psi_i]^T$ describes the attitude of the $i$–th rotorcraft in terms of classical 'roll', 'pitch', and 'yaw' angles, respectively. The following notation is adopted: if $\boldsymbol{w}$ is an arbitrary vector, its components are transformed from $\mathcal{F}_E$ to $\mathcal{F}_{Bi}$ through $\boldsymbol{w}_{Bi} = \boldsymbol{T}_{BE}(\boldsymbol{\alpha}_i)\, \boldsymbol{w}_E$. In what follows, the subscript $E$ will be dropped for simplicity.

### 2.2. Equations of motion

Let $\boldsymbol{r}_i = [r_{xi},\, r_{y_i},\, r_{zi}]^T$ be the position of the $i$–th multirotor and $\boldsymbol{v}_i = [v_{xi},\, v_{y_i},\, v_{zi}]^T$ its velocity with respect to the inertial frame. A suspended load with mass $m_l$ is connected in $P_l$ by a cable to the $i$–th multirotor, as depicted in Fig. 2.

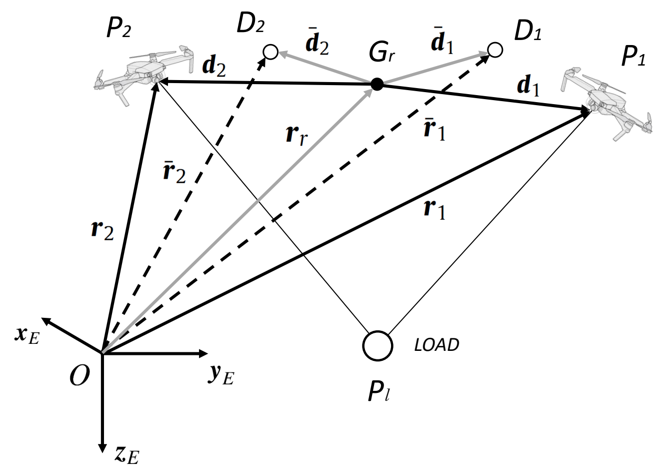


Figure 2: Definition of cable swing angles.

The dynamics of each agent as expressed in $\mathcal{F}_E$ is described by the following equations:

$$\text{(2)}\quad \dot{\boldsymbol{r}}_i = \boldsymbol{v}_i$$

$$\text{(3)}\quad \dot{\boldsymbol{v}}_i = \frac{1}{m}\left(m\,\boldsymbol{g} + \boldsymbol{f}_{di} + \boldsymbol{f}_{li} + \boldsymbol{u}_i\right)$$

where $m$ is mass of the rotorcraft, $\boldsymbol{g} = [0,\, 0,\, g]^T$ is local gravitational acceleration vector, $\boldsymbol{f}_{di}$ is vehicle aerodynamic drag, and $\boldsymbol{f}_{li}$ is the force induced by the load on the $i$–th rotorcraft through the cable. The total thrust vector $\boldsymbol{u}_i = [u_{xi},\, u_{y_i},\, u_{zi}]^T$, directed along $\boldsymbol{z}_{Bi}$ and pointing upwards, represents the only control input to Eq. (3). Provided $\rho$ is air density, $\boldsymbol{f}_{di}$ principally accounts for the contribution of rotorcraft frame, for which a simple flat–plate area model is proposed,

$$\text{(4)}\quad \boldsymbol{f}_{di} = -\frac{1}{2}\,\rho\left([A_x,\, A_y,\, A_z]\,\boldsymbol{v}_i\right)\boldsymbol{v}_i$$

where $A_x$, $A_y$, and $A_z$ are the equivalent flat plate drag areas facing the three body–frame axes of the $i$–th agent.

It is assumed that the $i$–th cable is directly connected to the center of gravity of the $i$–th multirotor, such that

$\boldsymbol{f}_{d\,i}$ has no effect on attitude motion. Payload dynamics is described by Newton–Euler equations projected in $\mathcal{F}_E$, namely:

$$(5)\quad \dot{\boldsymbol{v}}_l = \frac{1}{m_l}\left(m_l\,\boldsymbol{g} + \boldsymbol{f}_{dl} - \boldsymbol{f}_{l1} - \boldsymbol{f}_{l2}\right)$$

where $\boldsymbol{v}_l = [v_{xl},\, v_{y_l},\, v_{zl}]^T$ is payload velocity and $\boldsymbol{f}_{dl}$ is the aerodynamic force acting on the payload, here calculated as

$$(6)\quad \boldsymbol{f}_{dl} = -\frac{1}{2}\,\rho\,A_l\,C_{dl}\,\left\|\boldsymbol{v}_l\right\|\boldsymbol{v}_l$$

provided $C_{dl}$ is payload drag coefficient and $A_l$ is a reference area for drag computation. Each cable is mass–less and its aerodynamic drag is disregarded. Let $\boldsymbol{r}_l = [r_{xl},\, r_{y_l},\, r_{zl}]^T$ be the position of the load, obtained from

$$(7)\quad \dot{\boldsymbol{r}}_l = \boldsymbol{v}_l,$$

The vector describing the orientation and length of the $i$–th cable is $\boldsymbol{c}_i = \boldsymbol{r}_l - \boldsymbol{r}_i$. According to Hookes' model, the force $\boldsymbol{f}_{l_i}$ is calculated from the linear–elastic equation

$$(8)\quad \boldsymbol{f}_{l_i} = K\,\Delta L_i\,\hat{\boldsymbol{c}}_i$$

where $K$ is elastic constant, $L$ is nominal cable length, $\Delta L_i = \left\|\boldsymbol{c}_i\right\| - L$ is elastic deformation, and $\hat{\boldsymbol{c}}_i = \boldsymbol{c}_i/\left\|\boldsymbol{c}_i\right\|$.

### *2.3. Formation modeling*

Assume the $i$–th vehicle is required to keep a specified distance from a reference point $G_r$, identified by vector position $\boldsymbol{r}_r$ and moving with velocity $\boldsymbol{v}_r$. Provided $D_i$ is the $i$–th agent required position, identified by position vector $\bar{\boldsymbol{r}}_i$, it is

$$(9)\quad \boldsymbol{r}_r + \boldsymbol{d}_i = \boldsymbol{r}_i$$

and

$$(10)\quad \boldsymbol{r}_r + \bar{\boldsymbol{d}}_i = \bar{\boldsymbol{r}}_i$$

where $\boldsymbol{d}_i = [d_{xi},\, d_{y_i},\, d_{zi}]^T$ and $\bar{\boldsymbol{d}}_i = [\bar{d}_{x_i},\, \bar{d}_{y_i},\, \bar{d}_{z_i}]^T$ respectively indicate the current and the required relative distance between the $i$-th agent and the reference point. The following equation is derived:

$$(11)\quad \bar{\boldsymbol{d}}_i - \boldsymbol{d}_i = \bar{\boldsymbol{r}}_i - \boldsymbol{r}_i$$

Let $\dot{\bar{\boldsymbol{r}}}_i = \bar{\boldsymbol{v}}_i$ and consider Eq. (2). The time derivative of Eq. (11) yields:

$$(12)\quad \dot{\bar{\boldsymbol{d}}}_i - \dot{\boldsymbol{d}}_i = \bar{\boldsymbol{v}}_i - \boldsymbol{v}_i$$

where $\bar{\boldsymbol{v}}_i$ represents the desired velocity of the $i$–th vehicle. Assuming the desired velocity $\bar{\boldsymbol{v}}_i$ equals the velocity of the reference point $\boldsymbol{v}_r$, the position dynamics of the $i$–th vehicle with respect to the reference point becomes:

$$(13)\quad \dot{\boldsymbol{d}}_i = \dot{\bar{\boldsymbol{d}}}_i - \boldsymbol{v}_r + \boldsymbol{v}_i$$

Define $\boldsymbol{\delta}_i = \bar{\boldsymbol{d}}_i - \boldsymbol{d}_i$ and $\boldsymbol{\epsilon}_i = \boldsymbol{v}_r - \boldsymbol{v}_i$ as the relative position and trajectory error variables, respectively. By taking into account Eqs. (3) and (13), formation error dynamics results in

$$(14)\quad \dot{\boldsymbol{\delta}}_i = \boldsymbol{\epsilon}_i$$

$$(15)\quad \dot{\boldsymbol{\epsilon}}_i = -\boldsymbol{g} - \frac{1}{m}\left(\boldsymbol{f}_{d\,i} + \boldsymbol{f}_{l\,i} + \boldsymbol{u}_i\right) + \dot{\boldsymbol{v}}_r$$

The formation error dynamics defined above is extended to account for the residual degree of freedom related to payload oscillation. Let $G$ be the center of gravity of the complete system with total mass $M = 2\,m + m_l$ made of multirotors and payload, with position:

$$(16)\quad \boldsymbol{r} = \frac{1}{M}\left(m\,\boldsymbol{r}_1 + m\,\boldsymbol{r}_2 + m_l\,\boldsymbol{r}_l\right)$$

Assume the center of gravity $G$ is also required to track the reference point $G_r$, such that $\boldsymbol{\rho} = \boldsymbol{r}_r - \boldsymbol{r}$ is an error vector. Let $\boldsymbol{\sigma} = \dot{\boldsymbol{r}}_r - \dot{\boldsymbol{r}} = \boldsymbol{v}_r - \dot{\boldsymbol{r}}$, such that

$$(17)\quad \dot{\boldsymbol{\rho}} = \boldsymbol{\sigma}$$

Based on the definition of $G$ in Eq. (16), the dynamics of $\boldsymbol{\sigma}$ is derived from Eqs. (3) and (5) as

$$(18)\quad \dot{\boldsymbol{\sigma}} = \dot{\boldsymbol{v}}_r - \ddot{\boldsymbol{r}} = \dot{\boldsymbol{v}}_r - \boldsymbol{g} - \frac{1}{M}\left(\boldsymbol{u}_1 + \boldsymbol{u}_2\right)$$

With this in mind, the $i$–th elastic disturbance term defined in Eq. (8) and affecting Eq. (15) is be conveniently expressed as a function of errors $\delta_i$ and $\rho$. To this end, payload position is first expressed as a function of $\boldsymbol{r}$ from Eq. (16):

$$(19)\quad \boldsymbol{r}_l = \frac{1}{m_l}\left(-m\,\boldsymbol{r}_1 - m\boldsymbol{r}_2 + M\,\boldsymbol{r}\right)$$

Taking into account Eq. (9) and the definitions of formation error vectors, it follows $\boldsymbol{r}_i = \boldsymbol{r}_r + \boldsymbol{d}_i = \boldsymbol{r}_r + \bar{\boldsymbol{d}}_i - \boldsymbol{\delta}_i$ and $\boldsymbol{r} = \boldsymbol{r}_r - \boldsymbol{\rho}$ for $i = 1,\, 2$. By substitution into Eq. (19) one has

$$\begin{aligned}(20)\quad \boldsymbol{r}_l &= \frac{1}{m_l}\left[-m\left(\boldsymbol{r}_r + \bar{\boldsymbol{d}}_1 - \boldsymbol{\delta}_1\right) - m\left(\boldsymbol{r}_r + \bar{\boldsymbol{d}}_2 - \boldsymbol{\delta}_2\right)\right. \\ &\quad \left. M\left(\boldsymbol{r}_r - \boldsymbol{\rho}\right)\right] \\ &= \boldsymbol{r}_r - \frac{1}{m_l}\left[m\left(\bar{\boldsymbol{d}}_1 - \boldsymbol{\delta}_1\right) + m\left(\bar{\boldsymbol{d}}_2 - \boldsymbol{\delta}_2\right) + M\,\boldsymbol{\rho}\right]\end{aligned}$$

and the vector directed from rotorcraft $1$ to the payload becomes

$$\begin{aligned}(21)\quad \boldsymbol{c}_1 &= \boldsymbol{r}_l - \boldsymbol{r}_1 = \boldsymbol{r}_l - \left(\boldsymbol{r}_r + \bar{\boldsymbol{d}}_1 - \boldsymbol{\delta}_1\right) \\ &\quad - \frac{1}{m_l}\left[m\left(\bar{\boldsymbol{d}}_1 - \boldsymbol{\delta}_1\right) + m\left(\bar{\boldsymbol{d}}_2 - \boldsymbol{\delta}_2\right) + M\,\boldsymbol{\rho}\right] \\ &\quad - \bar{\boldsymbol{d}}_1 + \boldsymbol{\delta}_1 \\ &= -\left(\bar{\boldsymbol{d}}_1 - \boldsymbol{\delta}_1\right)\left(1 + \frac{m}{m_l}\right) - \left(\bar{\boldsymbol{d}}_2 - \boldsymbol{\delta}_2\right)\frac{m}{m_l} - \boldsymbol{\rho}\frac{M}{m_l}\end{aligned}$$

In the same way, it is:

$$(22)\quad \boldsymbol{c}_2 = -\left(\bar{\boldsymbol{d}}_2 - \boldsymbol{\delta}_2\right)\left(1 + \frac{m}{m_l}\right) - \left(\bar{\boldsymbol{d}}_1 - \boldsymbol{\delta}_1\right)\frac{m}{m_l} - \boldsymbol{\rho}\frac{M}{m_l}$$

### *2.4. Formation control*

The present section outlines the design of a controller to simultaneously perform 1) trajectory tracking, 2) position keeping, and 3) load swing stabilization. The application framework is defined by the following Assumption.

**Assumption 1** *It is supposed that:*

- *each vehicle has knowledge of both position and velocity of other objects in the formation, including the payload;*
- *inner–loop autopilot systems allow the $i$–th vehicle to track the desired control force $\boldsymbol{u}_i$ with sufficient accuracy;*
- *the controller is generated by disregarding the aerodynamic drag affecting both the rotorcraft and the payload.*

**Remark 1** The estimation of payload oscillatory state is a challenging issue that was recently investigated by one of the authors in the case of a single–agent system (Ref. 22). In particular, a method was validated to autonomously estimate the swing angle and rate in multicopter slung load applications, with no need to rely on sensors different from the available (typically low–cost) IMU. In such a framework accelerometer readings and dynamic model information are fused by means of a Fading Gaussian Deterministic (FGD) filter in the presence of model uncertainties and measurement errors. The adaptation of such method to the cooperative scenario still represents an ongoing research activity of the authors. However, other methods based on current technology can be envisaged to perform payload state determination. They include motion capture ground systems (Refs. 23 and 24), onboard visual detection devices (Refs. 25 and 26), or sensors that are fixed with respect to the load (Refs. 27, 28, and 29).

**Remark 2** The investigation of rotorcraft capability to track a desired control force does not represent the aim of the present analysis. Different control strategies can be designed to perform attitude control and generate the required thrust, that include standard PID techniques (Ref. 30), linear quadratic regulators (Ref. 31), active disturbance rejection controllers (Ref. 32), backstepping control or feedback linearization (Ref. 33), and sliding mode methods (Refs. 34 and 35). Regardless of control approach, it is a fundamental requirement that attitude regulation and thrust generation have a bandwidth significantly larger than the bandwidth of the cooperative transportation task. This is achieved by a proper selection of control gains while setting up safety constraints on maximum commanded attitude, angular rates, and accelerations. In a more general framework, the suspended load transportation problem is thus representative of a three–time–scale system if control signals are designed according to the approach outlined in the present paper: the time–scale that governs attitude dynamics is faster than that of combined formation–keeping and payload stabilization. The slowest dynamics is finally represented by trajectory–tracking task, as properly pointed out in Appendix 2.

Based on Assumption 1, a preliminary result is provided to characterize the formation geometry adopted in the present framework.

**Lemma 1** *Let $\boldsymbol{a} = [a_x,\, a_y,\, 0]^T$ be the prescribed mutual distance vector between the two agents of the formation, with components expressed in $\mathcal{F}_E$. Provided $a_x,\, a_y \in \mathbb{R}$ are selected such that $a = \sqrt{a_x^2 + a_y^2} < 2\,L$, it follows that desired formation geometry is defined by*

$$(23)\quad \bar{d}_{x_2} = -\bar{d}_{x_1} = a_x/2, \qquad \bar{d}_{y_2} = -\bar{d}_{y_1} = a_y/2,$$

*and*

$$(24)\quad \bar{d}_{z_2} = \bar{d}_{z_1} = -\frac{m_l}{2\,M}\sqrt{4\,\bar{L}^2 - a^2}$$

*where $\bar{L}$ is actual cable length of loaded formation, obtained as the only real positive solution of equation:*

$$(25)\quad p_0 + p_1\,\bar{L} + p_2\,\bar{L}^2 + p_3\,\bar{L}^3 + p_4\,\bar{L}^4 = 0$$

*that satisfies $\bar{L} > L$, where*

$$\begin{aligned}(26)\quad p_0 &= -K^2\,L^2\,a^2 \\ p_1 &= 2\,K^2\,L\,a^2 \\ p_2 &= 4\,K^2\left(L^2 - a^2/4\right) - m_l^2\,g^2 \\ p_3 &= -8\,K^2\,L \\ p_4 &= 4\,K^2\end{aligned}$$

**Proof** See Appendix 1.

Consider the formation geometry described in Lemma 1. Let $\boldsymbol{z}_i = [\boldsymbol{\delta}_i^T,\, \boldsymbol{\epsilon}_i^T]^T \in \mathbb{R}^6$ be the $i$–th extended error vector and define $\boldsymbol{x} = [\boldsymbol{\rho}^T,\, \boldsymbol{\sigma}^T]^T \in \mathbb{R}^6$. Provided $\boldsymbol{z} = [\boldsymbol{z}_1^T,\, \boldsymbol{z}_2^T]^T \in \mathbb{R}^{12}$, the dynamics of center of gravity tracking error $\boldsymbol{x}$ and formation error $\boldsymbol{z}$ are respectively expressed as

$$(27)\quad \dot{\boldsymbol{x}} = \boldsymbol{F}(\boldsymbol{x}, \boldsymbol{z}) + \boldsymbol{L}(t)$$

and

$$(28)\quad \dot{\boldsymbol{z}} = \boldsymbol{G}(\boldsymbol{x}, \boldsymbol{z}) + \boldsymbol{M}(t)$$

where $\boldsymbol{L}(t) = [\boldsymbol{0}_{1\times 3}\ \dot{\boldsymbol{v}}_r^T]^T \in \mathbb{R}^{6\times 1}$, $\boldsymbol{M}(t) = [\boldsymbol{L}^T\ \boldsymbol{L}^T]^T \in \mathbb{R}^{12\times 1}$,

$$(29)\quad \boldsymbol{F}(\boldsymbol{x}, \boldsymbol{z}) = \begin{bmatrix} \boldsymbol{\sigma} \\ -\boldsymbol{g} - \dfrac{1}{M}\,(\boldsymbol{u}_1 + \boldsymbol{u}_2) \end{bmatrix}$$

and

$$(30)\quad \boldsymbol{G}(\boldsymbol{x}, \boldsymbol{z}) = \begin{bmatrix} \boldsymbol{\epsilon}_1 \\ -\boldsymbol{g} - \dfrac{1}{m}\left[\left(1 - \dfrac{L}{\|\boldsymbol{c}_1\|}\right)\boldsymbol{c}_1 + \boldsymbol{u}_1\right] \\ \boldsymbol{\epsilon}_2 \\ -\boldsymbol{g} - \dfrac{1}{m}\left[\left(1 - \dfrac{L}{\|\boldsymbol{c}_2\|}\right)\boldsymbol{c}_2 + \boldsymbol{u}_2\right] \end{bmatrix}$$

are determined from Eqs. (14)–(22) under Assumption 1.

Let $\boldsymbol{K}_\delta = \mathrm{diag}(k_{\delta_x},\, k_{\delta_y},\, k_{\delta_z})$, $\boldsymbol{K}_\epsilon = \mathrm{diag}(k_{\epsilon_x},\, k_{\epsilon_y},\, k_{\epsilon_z})$, $\boldsymbol{K}_\rho = \mathrm{diag}(k_{\rho_x},\, k_{\rho_y},\, k_{\rho_z})$, and $\boldsymbol{K}_\sigma = \mathrm{diag}(k_{\sigma_x},\, k_{\sigma_y},\, k_{\sigma_z})$ be positive gain matrices. Define $\boldsymbol{K}_x = [\boldsymbol{K}_\rho\ \boldsymbol{K}_\sigma] \in \mathbb{R}^{3\times 6}$ and $\boldsymbol{K}_z = [\boldsymbol{K}_\delta\ \boldsymbol{K}_\epsilon] \in \mathbb{R}^{3\times 6}$. The following controller is proposed for $i = 1,\, 2$:

$$(31)\quad \boldsymbol{u}_i = \bar{\boldsymbol{u}}_i + \lambda_i\,\boldsymbol{\nu}_i + \mu_i\,\boldsymbol{\Sigma}\,\bar{\boldsymbol{d}}_i + m\,\boldsymbol{K}_z\,(\boldsymbol{z}_i + \boldsymbol{R}\,\boldsymbol{\alpha})$$

where $\bar{\boldsymbol{u}}_i$ is the trim contribution derived according to Lemma 1, $\boldsymbol{\Sigma} = \mathrm{diag}(m_l,\, m_l,\, M)$, and $\boldsymbol{R} = [\boldsymbol{I}_3 \,//\, \boldsymbol{0}_{3\times 3}] \in \mathbb{R}^{6\times 3}$ is a selection matrix obtained by vertical concatenation of $\boldsymbol{I}_3$ and $\boldsymbol{0}_{3\times 3}$. Functions $\lambda_1,\, \lambda_2,\, \mu_1,\, \mu_2 \in \mathbb{R}$ and $\boldsymbol{\nu}_1,\, \boldsymbol{\nu}_2 \in \mathbb{R}^3$ are defined as

$$(32)\quad \lambda_1 = K\,L\left(\frac{1}{m_l\,L} - \frac{1}{\|\boldsymbol{\nu}_1 + \boldsymbol{\Sigma}\,\bar{\boldsymbol{d}}_1\|}\right)$$

$$(33)\quad \lambda_2 = K\,L\left(\frac{1}{m_l\,L} - \frac{1}{\|\boldsymbol{\nu}_2 - \boldsymbol{\Sigma}\,\bar{\boldsymbol{d}}_2\|}\right)$$

$$(34)\quad \mu_1 = K\left(\frac{1}{\|\boldsymbol{\Sigma}\,\bar{\boldsymbol{d}}_1\|} - \frac{1}{\|\boldsymbol{\nu}_1 + \boldsymbol{\Sigma}\,\bar{\boldsymbol{d}}_1\|}\right)$$

$$(35)\quad \mu_2 = K\left(\frac{1}{\|\boldsymbol{\Sigma}\,\bar{\boldsymbol{d}}_2\|} - \frac{1}{\|\boldsymbol{\nu}_2 - \boldsymbol{\Sigma}\,\bar{\boldsymbol{d}}_2\|}\right)$$

$$(36)\quad \boldsymbol{\nu}_1 = M\,\boldsymbol{\rho} - (m + m_l)\,\boldsymbol{\delta}_1 - m\,\boldsymbol{\delta}_2$$

$$(37)\quad \boldsymbol{\nu}_2 = -M\,\boldsymbol{\rho} + (m + m_l)\,\boldsymbol{\delta}_2 + m\,\boldsymbol{\delta}_1$$

while $\boldsymbol{\alpha} \in \mathbb{R}^3$ is obtained as a solution of the the implicit equation

$$(38)\quad \boldsymbol{\alpha} = -\frac{m_l}{M}\boldsymbol{g} + \boldsymbol{K}_x\,\boldsymbol{x} + K\,L\left(\frac{\boldsymbol{\beta}_1}{\|\boldsymbol{\beta}_1\|} + \frac{\boldsymbol{\beta}_2}{\|\boldsymbol{\beta}_2\|} - \frac{\boldsymbol{\beta}_1 + \boldsymbol{\beta}_2}{m_l\,L}\right)$$

where $\boldsymbol{\beta}_1 = \boldsymbol{\alpha} + \boldsymbol{\rho} + \boldsymbol{\Sigma}\,\bar{\boldsymbol{d}}_1$ and $\boldsymbol{\beta}_2 = \boldsymbol{\alpha} + \boldsymbol{\rho} + \boldsymbol{\Sigma}\,\bar{\boldsymbol{d}}_2$.

Asymptotic stability for the origin $[\boldsymbol{x}^T\ \boldsymbol{z}^T]^T = \boldsymbol{0}_{18\times 1}$ of the closed–loop system in Eqs. (27)–(30) is addressed by the following theorem.

**Theorem 1** *Consider the system in Eqs.* (27)–(30) *with the control law in Eqs.* (31)–(38)*. Provided* $\dot{\boldsymbol{v}}_r \in L_2[0, \infty) \cap L_\infty[0, \infty)$*, there exist* $\boldsymbol{K}_x$ *and* $\boldsymbol{K}_z$ *such that* $\|\boldsymbol{x}\| \to 0$ *and* $\|\boldsymbol{z}\| \to 0$ *as* $t \to +\infty$*.*

**Proof** See Appendix 2.

## 3. RESULTS

The proposed control method is validated through numerical analysis. Simulations are performed by using Matlab® environment with a 4th–order Runge–Kutta solver frequency of $200$ Hz. The agents of the formation are two identical multirotors modeled as rigid bodies. The payload is assumed to be a point mass attached through a linear–elastic cable to a hook point $H$, coincident to rotorcraft center of gravity $CG$. The modeling follows the same approach and nomenclature adopted in Ref. 13. Relevant system parameters are listed in Table 1. The payload is affected by aerodynamic drag according to Eq. (6), provided $A_l = \pi\,R_l^2$ is frontal area of a sphere with radius $R_l = 0.5$ m and drag coefficient $C_{dl} = 0.5$. An octarotor platform is considered, characterized by a set of $4$ contra–rotating propulsion units (see Figure 1). The cross–shaped planar configuration is characterized by $STA_{R_1} = STA_{R_2} = STA_{R_5} = STA_{R_6} =$

$-STA_{R_3} = -STA_{R_4} = -STA_{R_7} = -STA_{R_8} = -0.690$ m, $BL_{R_1} = BL_{R_4} = BL_{R_5} = BL_{R_8} = -BL_{R_2} = -BL_{R_3} = -BL_{R_6} = -BL_{R_7} = 0.690$ m, $WL_{R_1} = WL_{R_2} = WL_{R_3} = WL_{R_4} = -0.024$ m, and $WL_{R_5} = WL_{R_6} = WL_{R_7} = WL_{R_8} = -0.238$ m.

Table 1: Multirotor slung–load system parameters

| Parameter | Symbol | Value | Units |
|---|---|---|---|
| Multirotor | | | |
| Mass | $m$ | 70 | kg |
| Center of gravity position | $STA_{CG} = BL_{CG}$ | 0 | m |
| | $WL_{CG}$ | -0.15 | m |
| Moments of inertia | $J_{11}$ | 10.61 | kg m$^2$ |
| | $J_{22}$ | 10.31 | kg m$^2$ |
| | $J_{33}$ | 19.74 | kg m$^2$ |
| | $J_{12}$ | 0.037 | kg m$^2$ |
| | $J_{13}$ | -0.043 | kg m$^2$ |
| | $J_{23}$ | -0.003 | kg m$^2$ |
| Center of pressure position | $STA_{CP} = BL_{CP}$ | 0 | m |
| | $WL_{CP}$ | -0.125 | m |
| Frame drag areas | $A_1 = A_2$ | 0.22 | m$^2$ |
| | $A_3$ | 1.03 | m$^2$ |
| Propeller | | | |
| Number of blades | $n_b$ | 2 | |
| Radius | $R$ | 0.5 | m |
| Mean aerodynamic chord | $\bar{c}$ | 0.086 | m |
| Chord @ $75\%\,R$ | $c_{75}$ | 0.103 | m |
| Lift curve slope | $a$ | 5.9 | rad$^{-1}$ |
| Pre–cone angle | $a_0$ | 0 | rad |
| Root pitch angle | $\theta_0$ | 0.7854 | rad |
| Total twist | $\theta_t$ | -0.6981 | rad |
| Load | | | |
| Mass | $m_l$ | 100 | kg |
| Reference area | $A_l$ | 0.785 | m$^2$ |
| Drag coefficient (sphere) | $C_{dl}$ | 0.5 | |
| Cable | | | |
| Nominal cable length | $L$ | 10 | m |
| Hooke's constant | $K$ | 130 | kN/m |
| Hook point position | $STA_H = BL_H$ | 0 | m |
| | $WL_H$ | $WL_{CG}$ | m |

Rotor forces and moments are calculated by means of Blade Element Momentum Theory, as well as the inflow related to the generation of thrust. With respect to the thrust and torque contributions only, a simplified model is proposed as in Ref. 13, such that:

$$T_j = k_T\,\Omega_j^2, \quad Q_j = k_Q\,\Omega_j^2 \tag{39}$$

where $k_T = \gamma\,\bar{k}_T$ and $k_Q = \gamma\,\bar{k}_Q$. $\bar{k}_T$ and $\bar{k}_Q$ are positive constants determined experimentally at air density $\bar{\rho}$ while $\gamma = \rho/\bar{\rho}$ is a density scaling parameter. In the present case, upper rotors (1–4) are characterized by $\bar{k}_T\big|_{up} = 2.90 \cdot 10^{-3}$ N/(rad/s)$^2$ while lower rotors (5–8) present $\bar{k}_T\big|_{down} = 2.20 \cdot 10^{-3}$ N/(rad/s)$^2$, accounting for reduced efficiency due to upper rotors wake interaction (Ref. 36). Finally, $\bar{k}_Q = 1.25 \cdot 10^{-4}$ Nm/(rad/s)$^2$ at the reference density $\bar{\rho} = 1.1229$ kg/m$^3$. The inflow iterative scheme is solved according to *fzero* Matlab® routine by Dekker with initial condition on the induced speed equal to $-10$ m/s (Ref. 37). Air parameters are calculated from the International Standard Atmosphere (ISA) model as a function of rotorcraft altitude (Ref. 38).

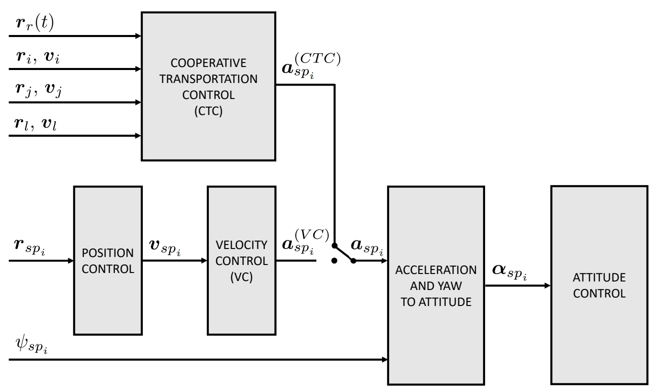


Figure 3: $i$–th multirotor control scheme based on PX4 autopilot architecture (Ref. 39).

Guidance, navigation, and control tasks are performed, without loss of generality, through a cascaded controller based on PX4 architecture and notation (Ref. 39). The control solution is assumed to stabilize the $i$–th multirotor according to different flight modes that include the tracking of an Earth–fixed set–point position $\boldsymbol{p}_{sp_i}$, velocity $\boldsymbol{v}_{sp_i}$, or acceleration $\boldsymbol{a}_{sp_i}$ (see Figure 3, where $\boldsymbol{a}_{sp_i}^{(VC)}$ is the acceleration set–point generated by Velocity Controller). In this framework, desired acceleration for the $i$–th multirotor is obtained as $\boldsymbol{a}_{sp_i} = \boldsymbol{a}_{sp_i}^{(CTC)} = \boldsymbol{u}_i/m$, where $\boldsymbol{u}_i$ is calculated according to the Cooperative Transportation Controller (CTC) in Eq. (31). Provided a detailed analysis of PX4 control functions is out of the scope of the present paper, it is supposed that inner–loop stabilization of attitude parameters is performed with prescribed requirements in terms of accuracy and rapidity, according to Remark 2. In order to simulate the effects of sensor noise on attitude control, zero–mean Gaussian white noise is added to each Euler angle and angular velocity measurement, with standard deviations $\sigma_\alpha = 0.5$ deg and $\sigma_\omega = 0.1$ deg/s, respectively. Control signals are generated at a sampling frequency of $100$ Hz.

Desired formation geometry is defined by $\boldsymbol{a} = [0,\, -10,\, 0]^T$. With this in mind, Lemma 1 gives $a = 10$ m, $\bar{d}_{x_2} = -\bar{d}_{x_1} = 0$ m, and $\bar{d}_{y_2} = -\bar{d}_{y_1} = -5$ m. Coefficients in Eq. (26) result to be $p_0 = -1.69 \cdot 10^{14}$ N$^2$m$^2$, $p_1 = 3.38 \cdot 10^{13}$ N$^2$m, $p_2 = 5.07 \cdot 10^{12}$ N$^2$, $p_3 = -1.352 \cdot 10^{12}$ N$^2$/m, and $p_4 = 6.76 \cdot 10^{10}$ N$^2$/m$^2$. As predicted by theory, $4$ real distinct solutions are provided ($3$ positive, $1$ negative). The only solution that satisfies $\bar{L} > L$ is $\bar{L} = 10.0044$ m, related to $\overline{\Delta L} = \bar{L} - L = 0.0044$ m cable elongation. Given $\bar{L}$, one derives $\bar{d}_{z_2} = \bar{d}_{z_1} = -3.6105$ m from Eq. (24), where $M = 2\,m + m_l = 240$ kg. From Eqs. (44) and (45) it is $\bar{\boldsymbol{c}}_1 = [0,\, -5,\, 8.6653]^T$ m and $\bar{\boldsymbol{c}}_2 = [0,\, 5,\, 8.6653]^T$ m, such that the unit vectors aligned with cable $1$ and cable $2$ are, respectively, $\hat{\bar{\boldsymbol{c}}}_1 = [0,\, -0.4998,\, 0.8662]^T$ and $\hat{\bar{\boldsymbol{c}}}_2 = [0,\, 0.4998,\, 0.8662]^T$. Trim forces are finally derived according to Eq. (47), where $\bar{\boldsymbol{u}}_1 = [0,\, 282.93,\, -1\,176.80]^T$ N and $\bar{\boldsymbol{u}}_2 = [0,\, -282.93,\, -1\,176.80]^T$ N. Based on simple geometric considerations, desired attitude of vehicles results to be $\boldsymbol{\alpha}_{SP_2} = -\boldsymbol{\alpha}_{SP_1} = -[\arctan\left(-\bar{u}_{y_1}/\bar{u}_{z_1}\right),\, 0,\, 0]^T = [-0.2359,\, 0,\, 0]^T$ rad, provided $\psi_{sp_2} = \psi_{sp_1} = 0$ rad. Control gain matrices are $\boldsymbol{K}_\delta = 4 \cdot \boldsymbol{I}_3$ 1/s$^2$, $\boldsymbol{K}_\epsilon = 3 \cdot \boldsymbol{I}_3$ 1/s, $\boldsymbol{K}_\rho = \mathrm{diag}(2.5,\, 2.5,\, 2500)$ 1/s$^2$, and $\boldsymbol{K}_\sigma = \boldsymbol{I}_3$ 1/s. It is noted that, for the given selection of control gain matrices, the eigenvalues of $\boldsymbol{H}$ in Eq. (58) (degenerate slow subsystem) are $-0.5 \pm 1.5\,i$ with multiplicity $2$ and $-0.5 \pm 50\,i$. On the other hand, the eigenvalues of $\bar{\boldsymbol{H}}$ in Eq. (60) (boundary–layer fast subsystem) are given by $-1.5 \pm 1.323\,i$, with multiplicity $3$. In order to avoid the generation of unusual attitudes and safely stabilize the vertical channel a bound is set on the third component of $\boldsymbol{u}_i$, such that $|u_{z_i} - \bar{u}_{z_i}|/\bar{u}_{z_i} \leq 10\%$. With respect to Eq. (38), a nonlinear system solver based on Levenberg–Marquardt method is implemented through the Matlab® routine *fsolve*, initialized with null first–guess solution (Ref. 40).

At time $t_0 = 0$ s the multirotors are required to leave the initial state defined by $\boldsymbol{r}_1(0) = [0,\, 5,\, -15]^T$ m, $\boldsymbol{r}_2(0) = [0,\, -5,\, -15]^T$ m, and $\boldsymbol{v}_1(0) = \boldsymbol{v}_2(0) = [0,\, 0,\, 0]^T$ m/s, with the payload at rest. In such a condition, payload position is given by $\boldsymbol{p}_l(0) = [0,\, 0,\, -6.3347]^T$ m and formation center of gravity is identified by $\boldsymbol{r}(0) = [0,\, 0,\, -11.3895]^T$ m. For $t > t_0$ the reference point is a constant equal to $\boldsymbol{r}_r(t) = \boldsymbol{r}(0) + [10,\, 0,\, 0]^T$ m. Based on the expected asymptotic nature of convergence, the maneuver is assumed to be concluded at time $t_m$ when $\left\|[\boldsymbol{x}^T\ \boldsymbol{z}^T]^T\right\| < 0.25$.

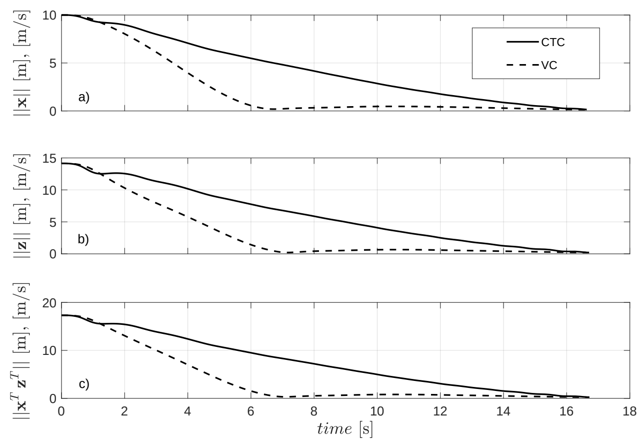


Figure 4: System stabilization in the presence of commanded acceleration as generated by cooperative transportation controller (CTC) and velocity controller (VC).

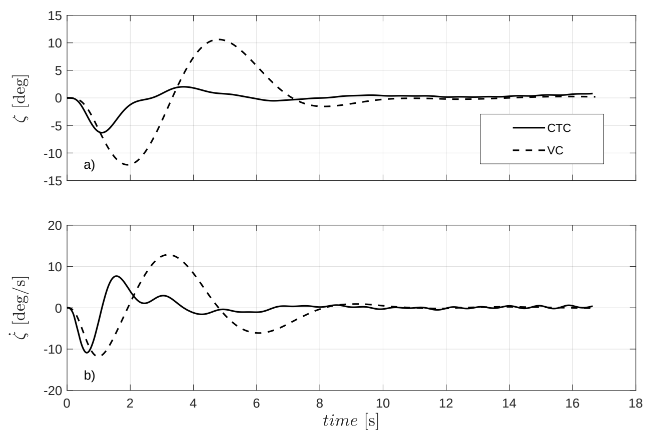


Figure 5: Oscillation angle and rate in the presence of commanded acceleration as generated by cooperative transportation controller (CTC) and velocity controller (VC).

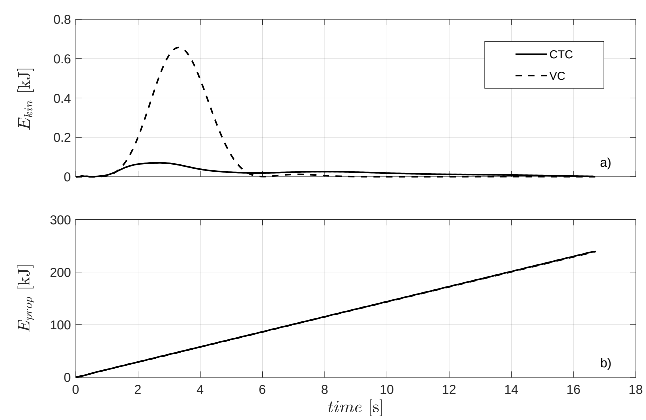


Figure 6: System energy contributions in the presence of commanded acceleration as generated by cooperative transportation controller (CTC) and velocity controller (VC).

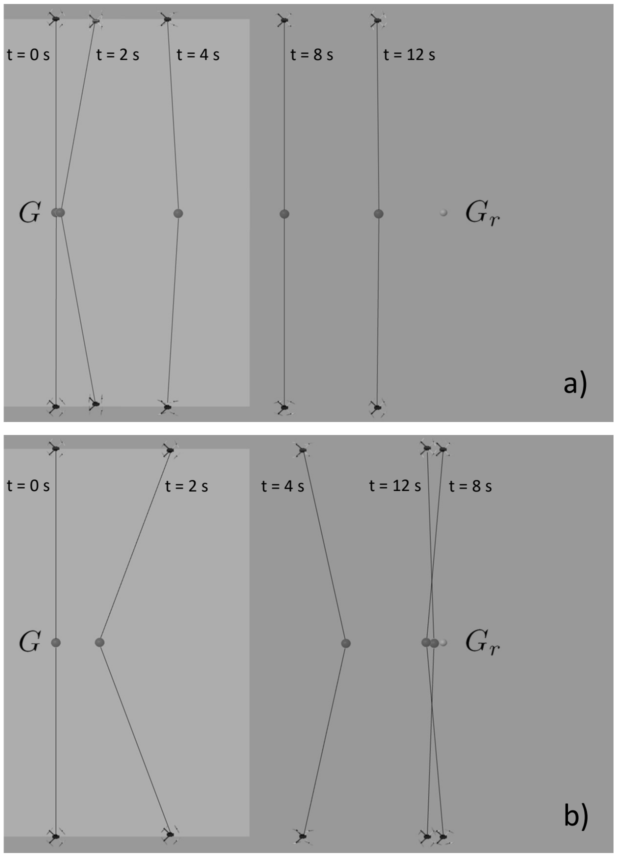


Figure 7: Formation geometry over the horizontal plane $\boldsymbol{x}_E - \boldsymbol{y}_E$ in the presence of commanded acceleration as generated by a) cooperative transportation controller (CTC) and b) velocity controller (VC).

Simulation results are summarized in Figures 4–6 (solid lines). In Figure 4 the evolution of both the slow and the fast subsystem variables is analyzed, showing convergence to the origin with $t_m = 16.6$ s. In Figure 5 payload state is characterized in terms of oscillation angle $\zeta$ and rate $\dot{\zeta}$, provided $\zeta$ is defined by the intersection of 1) the local–vertical plane that contains the multirotors (plane 1) and 2) the plane that contains all the objects of the formation, including the payload (plane 2). Given $\hat{\boldsymbol{c}}_1$ and $\hat{\boldsymbol{c}}_2$, the unit vector orthogonal to plane 2 is obtained as $\boldsymbol{e}_\perp = (\hat{\boldsymbol{c}}_2 \times \hat{\boldsymbol{c}}_1) / \|\hat{\boldsymbol{c}}_2 \times \hat{\boldsymbol{c}}_1\|$. Oscillation angle is finally calculated as $\zeta = -\arcsin(\boldsymbol{e}_{\perp z})$, provided $\boldsymbol{e}_{\perp z}$ is the third component of $\boldsymbol{e}_\perp$ as expressed in $\mathcal{F}_E$. According to the selected convention, a positive oscillation angle is obtained from positive rotation about vector $\boldsymbol{r}_1 - \boldsymbol{r}_2$. The integral quantity

(40) $$I_\zeta(t_m) = \int_0^{t_m} |\zeta(s)|\, ds$$

is also used to provide an indication of how much and how long plane 2 remains inclined with respect to plane 1. In a similar manner, the integral quantity

(41) $$I_{\dot{\zeta}}(t_m) = \int_0^{t_m} |\dot{\zeta}(s)|\, ds$$

is adopted as a performance index characterizing the swing rate during the entire maneuver. In the present case, it is $I_\zeta(t_m) = 14$ deg s and $I_{\dot{\zeta}}(t_m) = 19.53$ deg. In Figure 6.a kinetic energy $E_{kin} = 0.5\, \boldsymbol{v}_l^T \boldsymbol{v}_l$ of payload only is depicted as a function of time, being contributed by simultaneous payload swing motion and formation speed stabilization. In Figure 6.b propulsive energy delivered by multirotor 1 for all $t \in [0,\, t_m]$ is depicted. In the present framework, $E_{prop} = E_{prop}(t)$ represents the total mechanical energy delivered by electrical motors to propellers between $t = 0$ and $t$, for all $t \in [0,\, t_m]$, evaluated from the integral

(42) $$E_{prop}(t) = \int_0^t \sum_{i=1}^{8} P_{sh\,i}(s)\, ds$$

where $P_{sh\,i} = Q_i\, \Omega_i$ is the output shaft power generated by the $i$–th motor, obtained as the product of required torque $Q_i$ and angular rate $\Omega_i$, under the assumption of null friction torque. At the end of the proposed maneuver propulsive energy results to be $E_{prop}(t_m) = 238.90$ kJ, with average mechanical power calculated as $E_{prop}(t_m)/t_m = 14.36$ kW.

To get a better insight into the performance of the proposed controller, an alternative stabilization method is discussed for the same simulation case. Taking into account Figure 3, it is assumed that set–point acceleration of vehicle $i$ is generated by velocity controller rather than by cooperative transportation algorithm, namely $\boldsymbol{a}_{sp_i} = \boldsymbol{a}_{sp_i}^{VC}$. The set–point position to be achieved by the $i$–th agent is thus assigned as $\boldsymbol{p}_{sp_i} = \boldsymbol{p}_i(0) + [10,\, 0,\, 0]^T$. Position and velocity controller are tuned to allow the maneuver to be concluded in about the same time $t_m$ obtained above. Simulation results are also reported in Figures 4–6 for comparison (dotted lines). In this case $t_m = 16.7$ s and propulsive energy is not significantly altered, provided $E_{prop}(t_m) = 239.29$ kJ and the average mechanical power is $E_{prop}(t_m)/t_m = 14.31$ kW. Convergence is however obtained at the cost of increased values of performance indicators such as $I_\zeta(t_m) = 49.26$ deg s and $I_{\dot{\zeta}}(t_m) = 49.22$ deg ($+251.9\%$ and $+152.0\%$, respectively). Figure 7 finally resumes formation configuration at time instants $t = 0,\, 2,\, 4,\, 8,\, 12$ s over the horizontal plane $\boldsymbol{x}_E - \boldsymbol{y}_E$, according to the two approaches. It is evident how standard VC method is more aggressive in achieving the desired position at the cost of more pronounced oscillations (in this respect, see the rapid reduction of $\|\boldsymbol{z}\|$ in Figure 4). On the other hand, CTC determines a suitable compromise between stabilization tasks, allowing the maneuver to be concluded at the same time but with improved oscillation behavior.

## 4. CONCLUSIONS

This paper presents a methodology for cooperative load transportation by two rotorcraft. The proposed approach allows the lifting vehicles to perform trajectory–tracking and active payload swing stabilization according to a formation control formulation. The stability of the closed–loop system is addressed in the framework of two–time–scale analysis, provided the fast dynamics develops with formation geometry stabilization and payload swing damping while the slow dynamics is related to the trajectory–tracking task. Although the controller is generated for a nominal formation made of three point–masses, the application to a realistic simulation scenario with model uncertainties and measurement noise prove the effectiveness of the approach. A comparison is finally provided in the same scenario with the simple case when each agent is stabilized on a prescribed trajectory according to a standard controller, with no direct control on payload oscillations. In such a case, strong reduction of payload positioning accuracy is shown, with evident degradation of both swing angle and rate performance indexes. The approach can be extended to different rotorcraft configurations and requires the knowledge of a very–limited set of system parameters, while successfully encompassing the prescription of flying qualities. Finally, the physical interpretation of the control laws allows for a preliminary sizing of control gains based on the basic results of singular perturbation theory.

## 5. APPENDIX 1: PROOF OF LEMMA 1

The hypotheses in Lemma 1 and the definition of error $\boldsymbol{\rho}$ uniquely determine desired formation geometry, which is depicted in Figure 8. When the $i$–th agent reaches the desired position $D_i$ ($\boldsymbol{\delta}_i = \mathbf{0}_{3\times1}$, $\boldsymbol{\epsilon}_i = \mathbf{0}_{3\times1}$, $i = 1, 2$) and the formation center of gravity $G$ exactly tracks $G_r$ ($\boldsymbol{\rho} = \mathbf{0}_{3\times1}$, $\boldsymbol{\sigma} = \mathbf{0}_{3\times1}$), all elements $P_1$, $P_2$, $P_l$, and $G$ lie on a local vertical plane and the relative distance vectors $\boldsymbol{d}_1 = \bar{\boldsymbol{d}}_1$ and $\boldsymbol{d}_2 = \bar{\boldsymbol{d}}_2$ are organized according to a symmetric configuration that makes the derivation of results in Eq. (23) straightforward. In order to evaluate $\bar{d}_{z_1}$ and $\bar{d}_{z_2}$, the equilibrium of forces acting on the payload along the local vertical is analyzed. To this end, let $\left\|\bar{\boldsymbol{f}}_{l_i}\right\| = K\,\overline{\Delta L}$ be the $i$–th elastic force intensity in the equilibrium condition (see Eq. (8)), where $\overline{\Delta L} = \bar{L} - L$ and $\bar{L}$ are, respectively, desired cable elongation and length. Taking into account Eq. (5), it is

$$(43)\quad 2\,K\,\overline{\Delta L}\,\cos\bar{\xi} = m_l\,g$$

where $\bar{\xi} = \cos^{-1}(c/\bar{L})$ is the desired cable inclination with respect to the local vertical, with $c = \sqrt{\bar{L}^2 - (a/2)^2}$. Then Eq. (43) provides, after manipulation, Eqs. (25) and (26). Provided $p_2 > 0$, which occurs for values of practical application, the sequence of signs for the polynomial in Eq. (25) is $-++-+$. According to Descartes' rule three real positive solutions and one real negative solution are derived (Ref. 41). The only positive solution which is representative of the case where $\overline{\Delta L} > 0$ and the payload lies below the rotorcraft is the largest one, which can be determined analytically or by means of a root–finding numerical algorithm (Refs. 42 and 43).

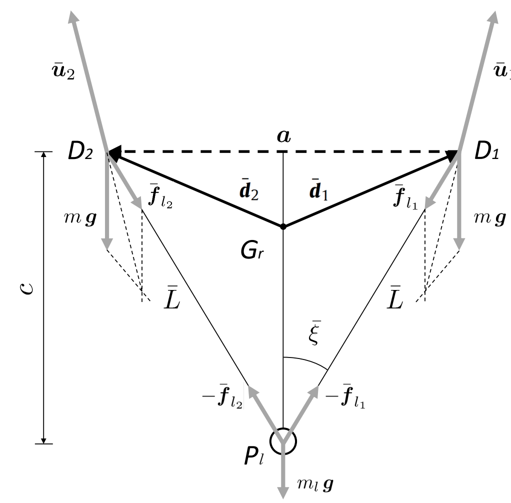


Figure 8: Desired formation geometry (relative distance $a$ is assigned).

Let $\bar{\boldsymbol{c}}_i$ be cable orientation vector in the equilibrium condition. From Eq. (21) it is

$$(44)\quad \bar{\boldsymbol{c}}_1 = -\bar{\boldsymbol{d}}_1\left(1 + \frac{m}{m_l}\right) - \bar{\boldsymbol{d}}_2\frac{m}{m_l}$$

and

$$(45)\quad \bar{\boldsymbol{c}}_2 = -\bar{\boldsymbol{d}}_2\left(1 + \frac{m}{m_l}\right) - \bar{\boldsymbol{d}}_1\frac{m}{m_l}$$

It is noted that parameter $c > 0$ in Figure 8 represents the third component of both $\bar{\boldsymbol{c}}_1$ and $\bar{\boldsymbol{c}}_2$. With this in mind, Eq. (44) provides

$$(46)\quad c = -\bar{d}_{z_1}\left(1 + \frac{m}{m_l}\right) - \bar{d}_{z_2}\frac{m}{m_l} = -\bar{d}_{z_1}\frac{M}{m_l}$$

with the knowledge that $\bar{d}_{z_2} = \bar{d}_{z_1}$. By equating the right–hand side of Eq. (46) to the expression of $c$ obtained from the analysis of right triangles in Figure 8, one finally derives the result in Eq. (24).

As a by–product of Lemma 1, the trim control forces $\bar{\boldsymbol{u}}_1$ and $\bar{\boldsymbol{u}}_2$ required for the rotorcraft to maintain the considered formation geometry are also derived. Static equilibrium from From Eq. (3) gives:

$$\bar{\boldsymbol{u}}_i = -m\,\boldsymbol{g} - \bar{\boldsymbol{f}}_{l_i} = -m\,\boldsymbol{g} - K\,\overline{\Delta L}\,\hat{\bar{\boldsymbol{c}}}_i \tag{47}$$

where $\hat{\bar{\boldsymbol{c}}}_i = \bar{\boldsymbol{c}}_i / \|\bar{\boldsymbol{c}}_i\|$ is calculated for $i = 1, 2$ by taking into account Eqs. (44) and (45).

## 6. APPENDIX 2: PROOF OF THEOREM 1

First the exponential stability of $[\boldsymbol{x}^T\,\boldsymbol{z}^T]^T = \mathbf{0}_{18\times1}$ is addressed in the case when $\dot{\boldsymbol{v}}_r = \mathbf{0}_{3\times1}$. Equations (27)–(30) with the control law in Eqs. (31)–(38) provide:

$$\boldsymbol{F}(\boldsymbol{x},\boldsymbol{z}) = \begin{bmatrix} \boldsymbol{\sigma} \\ -\boldsymbol{g} - \dfrac{1}{M}\Big[\bar{\boldsymbol{u}}_1 + \bar{\boldsymbol{u}}_2 + \lambda_1\,\boldsymbol{\nu}_1 + \lambda_2\,\boldsymbol{\nu}_2 \\ \quad + \mu_1\,\boldsymbol{\Sigma}\,\bar{\boldsymbol{d}}_1 + \mu_2\,\boldsymbol{\Sigma}\,\bar{\boldsymbol{d}}_2 \\ \quad + 2\,m\,\boldsymbol{K}_z\,\boldsymbol{R}\,\boldsymbol{\alpha} + m\,\boldsymbol{K}_z\,(\boldsymbol{z}_1 + \boldsymbol{z}_2)\Big] \end{bmatrix} \tag{48}$$

and

$$\boldsymbol{G}(\boldsymbol{x},\boldsymbol{z}) = \begin{bmatrix} \boldsymbol{\epsilon}_1 \\ -\boldsymbol{g} - \dfrac{1}{m}\Big[\Big(1 - \dfrac{L}{\|\boldsymbol{c}_1\|}\Big)\,\boldsymbol{c}_1 + \bar{\boldsymbol{u}}_1 + \lambda_1\,\boldsymbol{\nu}_1 \\ \quad + \mu_1\,\boldsymbol{\Sigma}\,\bar{\boldsymbol{d}}_1 + m\,\boldsymbol{K}_z\,(\boldsymbol{z}_1 + \boldsymbol{R}\,\boldsymbol{\alpha})\Big] \\ \boldsymbol{\epsilon}_2 \\ -\boldsymbol{g} - \dfrac{1}{m}\Big[\Big(1 - \dfrac{L}{\|\boldsymbol{c}_2\|}\Big)\,\boldsymbol{c}_2 + \bar{\boldsymbol{u}}_2 + \lambda_2\,\boldsymbol{\nu}_2 \\ \quad + \mu_2\,\boldsymbol{\Sigma}\,\bar{\boldsymbol{d}}_2 + m\,\boldsymbol{K}_z\,(\boldsymbol{z}_2 + \boldsymbol{R}\,\boldsymbol{\alpha})\Big] \end{bmatrix} \tag{49}$$

Taking into account Eqs. (21), (22), and the results obtained in Assumption 1, it can be shown that the latter equation simply becomes

$$\boldsymbol{G}(\boldsymbol{x},\boldsymbol{z}) = \bar{\boldsymbol{H}}\,\boldsymbol{z} - \boldsymbol{\Gamma}\,\gamma \tag{50}$$

where $\bar{\boldsymbol{H}}, \boldsymbol{\Gamma} \in \mathbb{R}^{12}$ are respectively given by

$$\bar{\boldsymbol{H}} = \left[\begin{array}{c|c} \begin{matrix}\boldsymbol{R}^T \\ -\boldsymbol{K}_z\end{matrix} & \mathbf{0}_{6\times6} \\ \hline \mathbf{0}_{6\times6} & \begin{matrix}\boldsymbol{R}^T \\ -\boldsymbol{K}_z\end{matrix} \end{array}\right] \tag{51}$$

and

$$\boldsymbol{\Gamma} = \left[\begin{array}{c|c} \begin{matrix}\mathbf{0}_{3\times6} \\ \boldsymbol{K}_z\,\boldsymbol{S}\end{matrix} & \mathbf{0}_{6\times6} \\ \hline \mathbf{0}_{6\times6} & \begin{matrix}\mathbf{0}_{3\times6} \\ \boldsymbol{K}_z\,\boldsymbol{S}\end{matrix} \end{array}\right] \tag{52}$$

where $\boldsymbol{\gamma} = [\mathbf{0}_{1\times3}\ \boldsymbol{\alpha}^T\,\mathbf{0}_{1\times3}\ \boldsymbol{\alpha}^T]^T \in \mathbb{R}^{12}$ and

$$\boldsymbol{S} = \begin{bmatrix} \mathbf{0}_{3\times3} & \boldsymbol{I}_3 \\ \boldsymbol{I}_3 & \mathbf{0}_{3\times3} \end{bmatrix} \tag{53}$$

Assume that a suitable selection of control gain matrices $\boldsymbol{K}_x$ and $\boldsymbol{K}_z$ forces the closed–loop system to exhibit a two–time–scale behavior. In the present framework, the scenario where formation–keeping and payload swing damping corresponds to the fast dynamics is considered, while trajectory tracking is related to the slow dynamics. In this way $\boldsymbol{x}$ and $\boldsymbol{z}$ are the vectors containing the slow and the fast variables, respectively. Also, it is noted that control signal in Eq. (38) is a function of the slow variable only, namely $\boldsymbol{\alpha} = \boldsymbol{\alpha}(\boldsymbol{x})$ and $\gamma = \gamma(\boldsymbol{x})$. With this in mind, the system in Eqs. (27), (28), (48), and (50) can be rewritten in the standard form:

$$\dot{\boldsymbol{x}} = \boldsymbol{F}(\boldsymbol{x},\boldsymbol{z},\varepsilon) \tag{54}$$

$$\varepsilon\,\dot{\boldsymbol{z}} = \boldsymbol{G}(\boldsymbol{x},\boldsymbol{z},\varepsilon) \tag{55}$$

where the artificial parameter $\varepsilon$ (whose nominal value is $1$) is inserted to represent $\boldsymbol{z}$ as the fast variable, according to the forced singular perturbation method described in Refs. 44 and 45.

Given the system in Eqs. (54) and (55), the proof follows from the stability results for singularly perturbed systems (see Theorem 11.4 in Ref. 21). In particular, it is $\boldsymbol{F}(\mathbf{0}_{6\times1},\mathbf{0}_{12\times1},\varepsilon) = \mathbf{0}_{6\times1}$ and $\boldsymbol{G}(\mathbf{0}_{6\times1},\mathbf{0}_{12\times1},\varepsilon) = \mathbf{0}_{12\times1}$. The equation $\mathbf{0}_{12\times1} = \boldsymbol{G}(\boldsymbol{x},\boldsymbol{z},0)$ has a single isolated root

$$\begin{aligned} \boldsymbol{z}_0 = \boldsymbol{h}(\boldsymbol{x}) &= \bar{\boldsymbol{H}}^{-1}\,\boldsymbol{\Gamma}\,\gamma(\boldsymbol{x}) \\ &= -[\boldsymbol{\alpha}^T(\boldsymbol{x})\ \mathbf{0}_{1\times3}\ \boldsymbol{\alpha}^T(\boldsymbol{x})\ \mathbf{0}_{1\times3}]^T \end{aligned} \tag{56}$$

that, given the definition of $\alpha$ in Eq. (38), satisfies $\boldsymbol{h}(\mathbf{0}_{6\times1}) = \mathbf{0}_{12\times1}$. Also, functions $\boldsymbol{F}$, $\boldsymbol{G}$, $\boldsymbol{h}$, and their partial derivatives are bounded up to the second order and $\boldsymbol{z}_0(t)$ represents the degenerate solution for $\boldsymbol{z}(t,\varepsilon)$, which is used in turn to evaluate the unperturbed problem:

$$\dot{\boldsymbol{x}}_0 = \boldsymbol{F}(\boldsymbol{x}_0,\boldsymbol{h}(\boldsymbol{x}_0),0) \tag{57}$$

and compute the degenerate solution $\boldsymbol{x}_0(t)$ for $\boldsymbol{x}(t,\varepsilon)$. In particular, Eq. (57) becomes:

$$\dot{\boldsymbol{x}}_0 = \boldsymbol{H}\,\boldsymbol{x}_0 \tag{58}$$

where $\boldsymbol{H} = [\boldsymbol{R}^T \,//\, -\boldsymbol{K}_x]$. Since $\boldsymbol{H}$ is a Hurwitz matrix, the origin of the degenerate system in Eq. (58) is exponentially stable. Consider now the change of variable $\boldsymbol{y} = \boldsymbol{z} - \boldsymbol{h}(\boldsymbol{x})$ and define $\tau = t/\varepsilon$. The boundary–layer system

$$\frac{d\boldsymbol{y}}{d\tau} = \boldsymbol{G}(\boldsymbol{x}, \boldsymbol{y} + \boldsymbol{h}(\boldsymbol{x}), 0) \tag{59}$$

assumes the form:

$$\frac{d\boldsymbol{y}}{d\tau} = \bar{\boldsymbol{H}}\,\boldsymbol{y} \tag{60}$$

which is independent of $x$ and whose origin is exponentially stable since $\bar{\boldsymbol{H}}$ is a Hurwitz matrix. Then, according to Theorem 11.4 in Ref. 21, there exists $\varepsilon^\star > 0$ such that for all $\varepsilon < \varepsilon^\star$, the origin of the nominal system in Eqs. (54) and (55) is exponentially stable.

Returning now to the complete system in Eqs. (27)–(30), note that it involves the extra term $\dot{\boldsymbol{v}}_r$. Since $\dot{\boldsymbol{v}}_r \in L_2[0,\infty) \cap L_\infty[0,\infty)$, one still obtains $\|\boldsymbol{x}\| \to 0$ and $\|\boldsymbol{z}\| \to 0$ as $t \to +\infty$ as a consequence of Lemma 1 in Ref. 46.

**Remark 3** The arguments reported in the proof of Theorem 1 establish robustness of exponential stability to the fast dynamics, provided $\varepsilon$ is sufficiently small to guarantee proper time–scale separation. Reduction of model order by neglecting the small parameter is representative of a singular perturbation condition, where the full singularly–perturbed model represents the actual system and the reduced (degenerate) model is the simplified version to be used in the analysis. When the origin of the reduced model is exponentially stable, the results in Ref. 21 assure that the origin of the actual system is exponentially stable, provided the neglected fast dynamics is sufficiently fast. Although the existence of a bound to $\varepsilon$ is proven, Theorem 11.4 in Ref. 21, which is based on converse Lyapunov methods, does not provide an explicit procedure for its determination. In the present case, where the insertion of $\varepsilon$ is representative of an artificial perturbation technique, the problem is shifted to the selection of control gains that suitably make the closed–loop system a multiple–time–scale system. However, the intermediate results reported in the proof of Theorem 1 allow to establish a direct relation between selected control gains and time–separation between dynamic modes. To this end, the comparison between the (slow) degenerate system in Eq. (58) and the (fast) boundary–layer system in Eq. (60) allows for direct analysis of respective matrix eigenvalues, with better insight into the separation mechanism.

## 7. ACKNOWLEDGMENTS

This study was carried out within the MOST - Sustainable Mobility National Research Center and received funding from the European Union Next-GenerationEU (PIANO NAZIONALE DI RIPRESA E RESILIENZA (PNRR) - MISSIONE 4 COMPONENTE 2, INVESTIMENTO 1.4 - D.D. 1033 17/06/2022, CN00000023). This manuscript reflects only the authors' views and opinions, neither the European Union nor the European Commission can be considered responsible for them.

## References

[1] E.L. de Angelis, F. Giulietti, G. Rossetti, G. Bellani, "Performance analysis and optimal sizing of electric multirotors", *Aerosp Sci Technol* 118 (2021) 107057, https://doi.org/10.1016/j.ast.2021.107057

[2] D. Lim, H. Kim, K. Yee, "Uncertainty propagation in flight performance of multirotor with parametric and model uncertainties", *Aerosp Sci Technol* 122 (2022) 107398, https://doi.org/10.1016/j.ast.2022.107398

[3] P.E.I. Pounds, D.R. Bersak, A.M. Dollar, "Grasping From the Air: Hovering Capture and Load Stability", in: Proc. of IEEE International Conference on Robotics and Automation, 2011, 2491–2498, https://doi.org/10.1109/ICRA.2011.5980314

[4] H. Chen, F. Quan, L. Fang, S. Zhang, "Aerial Grasping with a Lightweight Manipulator Based on Multi–Objective Optimization and Visual Compensation", *Sensors* 19 (2019) 4253, https://doi.org/10.3390/s19194253

[5] X. Li, J. Zhang, J. Han, "Trajectory planning of load transportation with multi–quadrotors based on reinforcement learning algorithm", *Aerosp Sci Technol* 116 (2021) 106887, https://doi.org/10.1016/j.ast.2021.106887

[6] P.E.I. Pounds, D. Bersak, A. Dollar, "Stability of small–scale UAV helicopters and quadrotors with added payload mass under PID control", *Auton Robot* 33 (2012) 129–142, https://doi.org/10.1007/s10514-012-9280-5

[7] I. Palunko, R. Fierro, P. Cruz, "Trajectory generation for swing–free maneuvers of a quadrotor with suspended payload: A dynamic programming approach", in: Proc. of 2012 IEEE International Conference on Robotics and Automation, 2012, 2691–2697, https://doi.org/10.1109/ICRA.2012.6225213

[8] S. Dai, T. Lee, D.S. Bernstein, “Adaptive Control of a Quadrotor UAV Transporting a Cable–Suspended load with Unknown Mass”, in: Proc. of the 53rd Conference on Decision and Control (CDC), 2014, 6149–6154, https://doi.org/10.1109/CDC.2014.7040352

[9] K. Sreenath, T. Lee, V. Kumar, “Geometric control and differential flatness of a quadrotor UAV with a cable–suspended load”, in: Proc. of the 52nd IEEE Conference on Decision and Control (CDC), 2013, 2269–2274, https://doi.org/10.1109/CDC.2013.6760219

[10] M.M. Nicotra, E. Garone, R. Naldi, L. Marconi, “Nested saturation control of an UAV carrying a suspended load”, in: Proc. of 2014 American Control Conference, 2014, 3585–3590, https://doi.org/10.1109/ACC.2014.6859222

[11] I.H.B. Pizetta, A.S. Brandão, M. Sarcinelli–Filho, “Modelling and control of a PVTOL quadrotor carrying a suspended load”, in: Proc. of 2015 International Conference on Unmanned Aircraft Systems (ICUAS), 2015, 444–450, https://doi.org/10.1109/ICUAS.2015.7152321

[12] J. Potter, W. Singhose, M. Costelloy, “Reducing swing of model helicopter sling load using input shaping”, in: Proc. of the 9th IEEE International Conference on Control and Automation (ICCA), 2011, 348–353, https://doi.org/10.1109/ICCA.2011.6138048

[13] E.L. de Angelis, F. Giulietti, “Stability and control issues of multirotor suspended load transportation: An analytical closed–form approach”, *Aerosp Sci Technol* 135 (2023) 108201, https://doi.org/10.1016/j.ast.2023.108201

[14] N. Michael, J. Fink, V. Kumar, “Cooperative manipulation and transportation with aerial robots”, *Auton Robot* 30 (2011) 73–86, https://doi.org/10.1007/s10514-010-9205-0

[15] T. Bacelar, J. Madeiras, R. Melicio, C. Cardeira, P. Oliveira, “On–board implementation and experimental validation of collaborative transportation of loads with multiple UAVs”, *Aerosp Sci Technol* 107 (2020) 106284, https://doi.org/10.1016/j.ast.2020.106284

[16] S.O. Ariyibi, O. Tekinalp, “Quaternion–based nonlinear attitude control of quadrotor formations carrying a slung load”, *Aerosp Sci Technol* 105 (2020) 105995, https://doi.org/10.1016/j.ast.2020.105995

[17] K. Klausen, C. Meissen, T.I. Fossen, M. Arcak, T.A. Johansen, “Cooperative Control for Multirotors Transporting an Unknown Suspended Load Under Environmental Disturbances”, *IEEE Trans Control Syst Technol* 28(2) (2020) 653–660, https://doi.org/10.1109/TCST.2018.2876518

[18] M. Tognon, C. Gabellieri, L. Pallottino, A. Franchi, “Aerial Co–Manipulation With Cables: The Role of Internal Force for Equilibria, Stability, and Passivity”, *IEEE Robot* 3(3) (2018) 2577–2583, https://doi.org/10.1109/LRA.2018.2803811

[19] E.L. de Angelis, F. Giulietti, G. Rossetti, “Multirotor aircraft formation flight control with collision avoidance capability”, *Aerosp Sci Technol* 77 (2018) 733–741, https://doi.org/10.1016/j.ast.2018.04.002

[20] E.L. de Angelis, F. Giulietti, G. Pipeleers, “Two–time–scale control of a multirotor aircraft for suspended load transportation”, *Aerosp Sci Technol* 84 (2019) 193–203, https://doi.org/10.1016/j.ast.2018.10.012

[21] H.K. Khalil, *Nonlinear Systems* (Third Edition), Prentice Hall, Upper Saddle River, NJ (2002), 456–459.

[22] E.L. de Angelis, “Swing angle estimation for multicopter slung load applications”, *Aerosp Sci Technol* 89 (2019) 264–274, https://doi.org/10.1016/j.ast.2019.04.014

[23] J.P. How, B. Behihke, A. Frank, D. Dale, J. Vian, “Realtime indoor autonomous vehicle test environment”, *IEEE Control Syst* 28(2) (2008) 51–64, https://doi.org/10.1109/MCS.2007.914691

[24] S. Lupashin, M. Hehn, M.W. Mueller, A.P. Schoellig, M. Sherback, R. D’Andrea, “A platform for aerial robotics research and demonstration: the flying machine arena”, *Mechatronics* 24(1) (2014) 41–54, https://doi.org/10.1016/j.mechatronics.2013.11.006

[25] M. Zürn, K. Morton, A. Heckmann, A. McFadyen, S. Notter, F. Gonzalez, “MPC controlled multirotor with suspended slung load: system architecture and visual load detection”, in: Proc. of IEEE Aerospace Conference, 2016, 1–11, https://doi.org/10.1109/AERO.2016.7500543

[26] M. Ebrahimi, M. Ghayour, S.M. Madani, A. Khoobroo, “Swing angle estimation for anti–sway overhead crane control using load cell”, *Int J Control Autom Syst* 9 (2011) 301–309, https://doi.org/10.1007/s12555-011-0212-5

[27] Y. Feng, J. Wang, "GPS RTK Performance Characteristics and Analysis", *J Glob Position Syst* 7(1) (2008), https://doi.org/10.5081/jgps.7.1.1

[28] Y.S. Kim, K.S. Hong, S.K. Sul, "Anti–Sway Control of Container Cranes: Inclinometer, Observer, and State Feedback", *Int J Control Autom Syst* 2(4) (2004) 435–449, https://doi.org/10.1.1.454.9911

[29] H. Paul, K. Ono, R. Ladig, K. Shimonomura, "A Multirotor Platform Employing a Three–Axis Vertical Articulated Robotic Arm for Aerial Manipulation Tasks", in: Proc. of IEEE/ASME International Conference on Advanced Intelligent Mechatronics (AIM), 2018, 478–485, https://doi.org/10.1109/AIM.2018.8452699

[30] A.A. Najm, I.K. Ibraheem, "Nonlinear PID controller design for a 6–DOF UAV quadrotor system", *Int J Eng Sci Technol* 22(4) (2019) 1087–1097, https://doi.org/10.1016/j.jestch.2019.02.005

[31] F. Rinaldi, S. Chiesa, F. Quagliotti, "Linear quadratic control for quadrotors UAVs dynamics and formation flight", *J Intell Robot Syst* 70(1) (2013) 203–220, https://doi.org/10.1007/s10846-012-9708-3

[32] Y. Zhang, Z. Chen, M. Sun, X. Zhang, "Trajectory tracking control of a quadrotor UAV based on sliding mode active disturbance rejection control", *Nonlinear Anal Model Control* 24(4) (2019) 545–560, https://doi.org/10.15388/NA.2019.4.4

[33] L. Zhou, J. Zhang, J. Dou, B. Wen, "A fuzzy adaptive backstepping control based on mass observer for trajectory tracking of a quadrotor UAV", *Int J Adapt Control Signal Process* 32(12) (2018) 1675–1693, https://doi.org/10.1002/acs.2937

[34] W. Gong, B. Li, Y. Yang, H. Ban, B. Xiao, "Fixed–time integral-type sliding mode control for the quadrotor UAV attitude stabilization under actuator failures", *Aerosp Sci Technol* 95 (2019) 105444, https://doi.org/10.1016/j.ast.2019.105444

[35] B. Gao, Y.J Liu, L. Liu, "Adaptive neural fault–tolerant control of a quadrotor UAV via fast terminal sliding mode", *Aerosp Sci Technol* 129 (2022) 107818, https://doi.org/10.1016/j.ast.2022.107818

[36] H.W. Kim, R.E. Brown, "A Comparison of Coaxial and Conventional Rotor Performance", *J Am Helicopter Soc* 55 (2010) 012004, 1–20, https://doi.org/10.4050/JAHS.55.012004

[37] G.E. Forsythe, M.A. Malcolm, C.B. Moler, *Computer Methods for Mathematical Computations*, Prentice–Hall, 1976.

[38] U.S. Government Printing Office, "U.S. Standard Atmosphere", NOAA-S/T 76-1562 (1976) 1–241.

[39] PX4 Development Team and Community, PX4 Autopilot User Guide (main), <`https://docs.px4.io/main/en/`> (accessed 11/23/2021).

[40] W.H. Press, B.P. Flannery, S.A. Teukolsky, W.T. Vetterling, *Numerical Recipes in C: The Art of Scientific Computing* (Second Edition), Cambridge University Press (1992), Ch. 15.5.

[41] D. Curtiss, Recent extensions of Descartes' rule of signs, *Annals of Maths* 19(4) (1918) 251–278.

[42] C.B. Boyer, U.C. Merzbach, *A History of Mathematics* (Third Edition), Wiley, Hoboken, NJ (2010), 255–259.

[43] W.H. Press, S.A. Teukolsky, W.T. Vetterling, B.P. Flannery, *Numerical recipes: the art of scientific computing* (Second Edition), Cambridge University Press (1992), Chs. 5, 9, and 10.

[44] D.S. Naidu, A.J. Calise, "Singular Perturbations and Time Scales in Guidance and Control of Aerospace Systems: A Survey", *J Guid Control Dyn* 24(6) (2001) 1057–1078, https://doi.org/10.2514/2.4830

[45] A. Narang–Siddarth, J. Valasek, *Nonlinear Time Scale Systems in Standard and Nonstandard Forms: Analysis and Control*, Society for Industrial and Applied Mathematics (2014), Ch. 1.

[46] R.W. Beard, J. Lawton, F.Y. Hadaegh, "A Coordination Architecture for Spacecraft Formation Control," *IEEE Trans Control Syst Technol*9(6) (2001) 777–790, doi: https://doi.org/10.1.1.137.8113